

The inner density profile of an elliptical galaxy at $z = 1.15$ from gravitational lensing

H. R. Stacey,^{1*} C. M. O’Riordan¹, S. Vegetti¹, D. M. Powell¹, M. W. Auger^{2,3}, and G. Despali⁴

¹Max Planck Institute for Astrophysics, Karl-Schwarzschild Str. 1, D-85748 Garching bei München, Germany

²Institute of Astronomy, University of Cambridge, Madingley Road, Cambridge CB3 0HA, UK

³Kavli Institute for Cosmology, University of Cambridge, Madingley Road, Cambridge CB3 0HA, UK

⁴Zentrum für Astronomie der Universität Heidelberg, Institut für Theoretische Astrophysik, Albert-Ueberle-Str. 2, 69120 Heidelberg, Germany

Accepted XXX. Received YYY; in original form ZZZ

ABSTRACT

The density profiles of lensing galaxies are typically parameterised by singular power-law models with a logarithmic slope close to isothermal ($\zeta = 2$). This is sufficient to fit the lensed emission near the Einstein radius, but may not be sufficient when extrapolated to smaller or larger radii if the large-scale density profile is more complex. Here, we consider a broken power-law model for the density profile of an elliptical galaxy at $z = 1.15$ using observations with the Atacama Large (sub-)Millimetre Array of the strong gravitational lens system SPT 0532–50. This is the first application of such a model to real data. We find the lensed emission is best fit by a density profile that is sub-isothermal ($\zeta = 1.87^{+0.02}_{-0.03}$) near the Einstein radius and steepens to super-isothermal ($\zeta = 2.14^{+0.03}_{-0.02}$) at around half the Einstein radius, demonstrating that the lensing data probes the mass distribution inside the region probed by the lensed images. Assuming that a broken power-law is the underlying truth, we find that a single power-law would result in a 10 ± 1 percent underestimate of the Hubble constant from time-delay cosmography. Our results suggest that a broken power-law could be useful for precision lens modelling and probing the structural evolution of elliptical galaxies.

Key words: gravitational lensing: strong – cosmology: dark matter – galaxies: evolution – galaxies: elliptical

1 INTRODUCTION

Galaxy-scale strong lenses are commonly modelled with a singular power-law ellipsoidal mass distribution (Treu 2010, for review). This has been shown to accurately describe the position and brightness of lensed images near the Einstein radius with a logarithmic slope that is typically close to isothermal (Auger et al. 2010). The assumption, therefore, is that the local density profile can be extrapolated to inner radii. However, the slope inferred from lensing alone has been found to disagree with inferences that include information from lens galaxy kinematics (Treu & Koopmans 2004; Birrer et al. 2016) or multi-source lensing (Sonnenfeld et al. 2012) which measures the average density profile over a larger range of radii, suggesting the mass profiles of galaxies are more complex (see also van de Ven et al. 2009). Furthermore, Enzi et al. (2020) and Kochanek (2020) found that, if the inner density profiles of galaxies deviates from a single power-law, constraints from a singular power-law lens model could result in significant systematic errors on the source size and Hubble constant (H_0).

The inner structure of galaxies is determined by the physical processes that guide their formation and evolution. Dark matter haloes can span a variety of inner density slopes: N-body simulations of Λ CDM haloes almost universally have an inner density described by $\rho \propto r^{-1}$ (cusps; Navarro et al. 1996), whilst alternative dark matter

models such as fuzzy or self-interacting dark matter can produce a constant inner density (cores; Yoshida et al. 2000; Burkert 2020). However, baryons strongly dominate in the centre of galaxies and can modify the distribution of dark matter. The accretion of gas may cause the centre of a halo to contract adiabatically (Blumenthal et al. 1986; Gnedin et al. 2011; Schaller et al. 2015), or the removal of gas by active galactic nuclei (AGN) or stellar feedback could cause it to adiabatically expand, creating a core (Martizzi et al. 2013; Pontzen & Governato 2012). A cored profile could also result from three-body interactions between supermassive black hole binaries and stars (Begelman et al. 1980; Quinlan 1996) or dynamical friction from subhalo accretion (Romano-Díaz et al. 2008). The interplay between self-interacting dark matter and baryons may result in cored or cuspy haloes, depending on the galaxy formation history (Despali et al. 2019; Vargya et al. 2021).

From the perspective of observations, there is controversy over the existence of cores: while there is a general consensus that profiles exist on cluster-scales (Sand et al. 2004; Newman et al. 2013; Collett et al. 2017), on galaxy-scales there have been claims of both cuspy and cored profiles (de Blok et al. 2001; Simon et al. 2003; Grillo 2012; Sonnenfeld et al. 2015; Pineda et al. 2017; Oldham & Auger 2018; Bouché et al. 2021).

Sensitivity of strong lensing data to the shape of the inner mass profile depends on the ellipticity of the lensing object, the number and extent of the images, and overall data quality. With a combination of theory and Hubble Space Telescope (HST) mock observations,

* E-mail: stacey@mpa-garching.mpg.de

O’Riordan et al. (2020, 2021) demonstrated that lensing constrains the mass profile of galaxies primarily via simple positional (i.e. astrometric) information and that the slope of a mass profile truncated inside the lensed images could be constrained by lensing data alone. The strength of this constraint improves with ellipticity and with the proximity of the images to the truncation radius. These principles extend to the broken power-law model we use here.

Another constraint on the inner density profile is via the lensed image (or lack, thereof) that forms at the Fermat maximum close to the centre of the lens. This image is strongly demagnified (Keeton 2003), but could be detected at radio/mm wavelengths where the lensing galaxy is not luminous and the source is sufficiently bright. Detection of the central image in two lens systems imply a steep inner profile resulting from a cuspy stellar distribution and central supermassive black hole (SMBH; Winn et al. 2004; Muller et al. 2020). The non-detection of central images in other cases is consistent with the constraints from detected central images, implying density profiles remain close to isothermal within ~ 100 pc (Rusin & Ma 2001; Quinn et al. 2016).

With the advent of the Atacama Large (sub-)Millimetre Array (ALMA), observations of gravitational lenses now present a promising avenue to investigate the inner density slope of early-type galaxies. At sub-mm wavelengths, as in the radio/mm, the lens is usually not luminous and lensed emission is unaffected by propagation effects. However, contrary to radio/mm, the source is typically more extended and structured, being associated with emission from dust in star-forming regions rather than an AGN core, so the central image is less susceptible to de-magnification (Hezaveh et al. 2015). Using ALMA observations of the lensed sub-mm galaxy SDP.81, Tamura et al. (2015) and Wong et al. (2015) found that the lack of a central image could be explained by the mass contributions from the observed (cored) stellar distribution and SMBH, albeit with a fixed or strong prior for the core radius.

In this work, we investigate SPT 0532–50: an early-type galaxy at $z_l = 1.15$ lensing a dusty star-forming galaxy at $z_s = 3.399$ (Vieira et al. 2013). Using observations with ALMA, we take advantage of an extended source (≈ 0.5 arcsec) to constrain the shape of the inner mass distribution without contamination from lens light. The paper is structured as follows. In Section 2 we describe the observations and data reduction. We give an overview of the lens modelling approach in Section 3 and present our findings in Section 4. We discuss the implications of our results for models of galaxy evolution and lens modelling systematics in Section 5. Section 6 is a summary and our outlook for future work.

Throughout, we assume the Planck Collaboration et al. (2016) flat Λ CDM cosmology with $H_0 = 67.8 \text{ km s}^{-1} \text{ Mpc}^{-1}$, $\Omega_M = 0.31$ and $\Omega_\Lambda = 0.69$.

2 DATA

2.1 ALMA data

SPT 0532–50 was observed with ALMA under project code (2016.1.01374.S, PI: Hezaveh) in antenna configurations with longest baseline 1.4 km, 4 km and 8.5 km. The data were correlated in four spectral windows each of 0.5 GHz at a central frequency of 350 GHz (1500 GHz rest-frame) with parallel linear polarisations (XX,YY). Observations were taken in four epochs on 16 Oct 2016, 11 Sept 2017, 16 Sept 2017, 19 Nov 2017. We did not use data from the first epoch with a longest baseline 1.4 km. The spectral set-up covered the rest-frame of a CO line, but only the line-free spectral windows were considered for the remainder of this experiment.

J0519–4546 was observed as the absolute flux calibrator and J0522–3627 was used as the spectral bandpass calibrator. Phase referencing to J0531–4827 was performed to correct time-dependent phase variations. The total integration time on SPT 0532–50 was about 3 hours.

We used the ALMA pipeline in the Common Astronomy Software Applications package (CASA; McMullin et al. 2007) to calibrate the data. The data were inspected to confirm the quality of the pipeline calibration and no further flagging was required. Self-calibration, using a solution interval of each observation length, was performed to correct the phase and amplitude offsets between epochs and improve the overall dynamic range of the data.

The measurement errors and weights were computed by subtracting subsequent visibilities in a time-series and taking the average in 1200s intervals, so as to avoid the effect of source structure in the noise estimation.

The deconvolved image of the data is shown in Fig. 1 (left). The very extended nature of the source, tidal tail features and high sub-mm luminosity strongly suggest that the source is an ongoing major merger.

2.2 HST data

HST observations of SPT 0532–50 were performed on 8 Oct 2011 with F110W (1.1 μm ; exposure time of 1312s) and F160W (1.6 μm ; exposure time of 1412s) filters (programme ID 12659). The data were calibrated using the ASTRODRIZZLE software and drizzled onto a pixel scale of 0.04 arcsec using a Gaussian kernel. A colour image is shown in Fig. 1 (right). No lensed emission is clearly detected, but there is some diffuse emission and a faint feature East of the lens that may be associated with the lens or the source.

3 MASS MODELLING

We used the pixellated lens modelling technique appropriate for interferometric data introduced in Powell et al. (2021) (see also Vegetti & Koopmans 2009; Rybak et al. 2015a; Rizzo et al. 2018). This method reconstructs the source emission on an Delaunay grid adapted to the lensing magnification. The model for the lensed emission is compared directly in the plane of the data via Fourier transform and the lens parameters are inferred within a Bayesian framework. We direct the reader to Powell et al. (2021) for a detailed explanation of the methodology.

Due to the observing frequencies and antenna size of ALMA, the antenna response may be significant for these data as the lens is a few arcsec from the phase centre. We correct for this effect in the lens modelling using a Gaussian function with half-power beam width of $1.13 \times \lambda/D$ ¹.

We consider an elliptical broken power-law (BPL) mass distribution that allows for different inner and outer logarithmic slopes. As the broken power-law is in 2D, the convergence is not smooth across the break radius, although the deflection angle is. As introduced by O’Riordan et al. (2021), the convergence of the BPL is defined as

$$\kappa(r) = \begin{cases} \kappa_B (r/r_B)^{t_1}, & r < r_B, \\ \kappa_B (r/r_B)^{t_2}, & r \geq r_B, \end{cases} \quad (1)$$

¹ ALMA Cycle 7 Technical Handbook https://arc.iram.fr/documents/cycle7/ALMA_Cycle7_Technical_Handbook.pdf

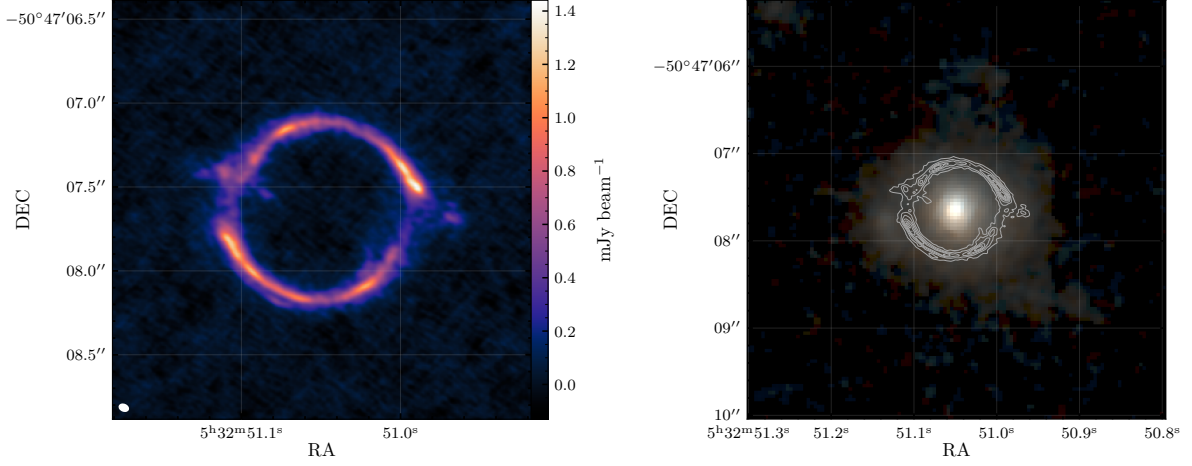


Figure 1. Left: 2.5×2.5 arcsec² deconvolved image of the 350 GHz (850 μ m) ALMA data with natural weighting of the visibilities. The synthesised beam has a FWHM of 37×53 mas and is shown in the lower left-hand corner. No emission from the lens is detected. Right: 5×5 arcsec² colour image of the lens from 1.1 μ m and 1.6 μ m HST imaging, drizzled with a pixel scale of 0.04 arcsec. The contours of the ALMA image are shown in grey, in units of 5σ . There is a faint feature East of the lens and general diffuse emission that may be associated with the lens or the source.

where κ_B is the convergence at the break radius, defined as

$$\kappa_B = \begin{cases} \frac{2-t_1}{2\nu^2[1+\delta_t(\nu^{t_2-2}-1)]}, & \nu < 1, \\ \frac{2-t_1}{2\nu^{t_1}}, & \nu \geq 1, \end{cases} \quad (2)$$

where r is the elliptical radius ($r = \sqrt{x^2 + y^2/q^2}$) and r_B is the elliptical break radius. $\delta_t = (2-t_1)/(2-t_2)$ and $\nu = r_B/b$, where b is $\sqrt{q}\theta_E$. The 2D logarithmic slope, t , is the equivalent of a 3D slope, ζ where $\zeta \equiv t - 1$. The free parameters of the model are the Einstein radius (θ_E), the axis ratio (q), the position angle (θ), the lens position relative to the phase centre (x_L, y_L), the inner and outer logarithmic slopes (ζ_1, ζ_2) and the break radius (r_B). We use the same model as an analogue for a cored single power-law by fixing the inner slope (note that this not equivalent to a softened cored power-law).

We note a luminous feature to the East of the main lens in the HST imaging. It is not clear whether this is lensed source emission (DSFGs are frequently found to have offset optical/UV emission, e.g. Rybak et al. 2015b) or a companion of the lensing galaxy (e.g. McKean et al. 2007). We attempted to include it in our lens model as a singular isothermal sphere, but it was not preferred by the data over the single lens (this is also suggested by the lack of significant external shear).

We consider whether the SMBH may contribute to the inner density profile by adding a point mass to the centre of the PL. The Einstein radius (θ_E) of a point mass (M_{BH}) is described by

$$\theta_E = \sqrt{\frac{4GM_{\text{BH}}}{c^2} \frac{D_{LS}}{D_L D_S}}, \quad (3)$$

where D_L , D_S and D_{LS} are the angular diameter distances to the lens, to the source and from lens to source, respectively.

We use nested sampling with MULTINEST (Feroz et al. 2013) to explore the multi-dimensional posterior distribution and calculate the Bayesian evidence for each of the considered models. We assume uniform priors for the lens parameters, with a uniform prior in log-space for the core radius (0.0001–0.1). The 2-dimensional posterior distributions of the lens parameters are shown in Fig. 3.

4 RESULTS

4.1 Inner density profile

The two-dimensional posterior distributions for the lens parameters from the PL and BPL models are shown in Fig. 3. A plot of the convergence and logarithmic slope profiles of these models is shown in Fig. 4. As can be seen from the variance in the convergence of the models probed by MULTINEST, the PL model suggests a core of < 0.01 arcsec (80 pc). We find that core sizes less than this value have no significant difference in the model evidence. A core radius of 0.05 arcsec (400 pc) is strongly disfavoured with a Bayes factor of 38 relative to the PL with a free core radius. The maximum *a-posteriori* PL model and source are shown in Fig. 2: we also show images for the model for a core radius of 0.05 which shows negative residuals from radial arcs and central image produced by the model that are not in agreement with the data. Note that these images are shown only for visualisation as the comparison with the data is performed in the uv plane.

We consider whether the steepness of the inner density profile could be produced by a conspiracy between the SMBH mass and a cored stellar mass distribution by adding a point mass to the centre of the PL. We find no significant change in the core radius (< 0.01 arcsec) and a mass of $2 \times 10^{10} M_{\odot}$ for the SMBH. However, given the typical stellar mass of lenses with similar Einstein radius ($\sim 10^{11} M_{\odot}$; Oldham & Auger 2018) we should expect a SMBH mass of just $\sim 10^8 M_{\odot}$ based on the $M_{\text{SMBH}}-M_{\text{bulge}}$ relation (Kormendy & Ho 2013). Therefore, we conclude the point mass represents a complexity in the large-scale radial density profile of the lens that can better investigated with the flexibility of the BPL model.

The posterior distributions of the BPL is shown alongside the PL model in Fig. 3. While the PL prefers a slope just slightly super-isothermal, the BPL model prefers a super-isothermal inner logarithmic slope ($\zeta_1 = 2.14^{+0.03}_{-0.02}$) and a sub-isothermal slope at the radius of the lensed images ($\zeta_2 = 1.87^{+0.02}_{-0.03}$) where the break occurs at around half the Einstein radius. Fig. 2 shows the maximum *a-posteriori* lens model for the BPL case: no negative residuals can be seen in the centre of the lens as the steeper density profile causes the inner radial arcs to be strongly demagnified. Interestingly, no external shear is preferred for the BPL model (or for PL+SMBH). This suggests

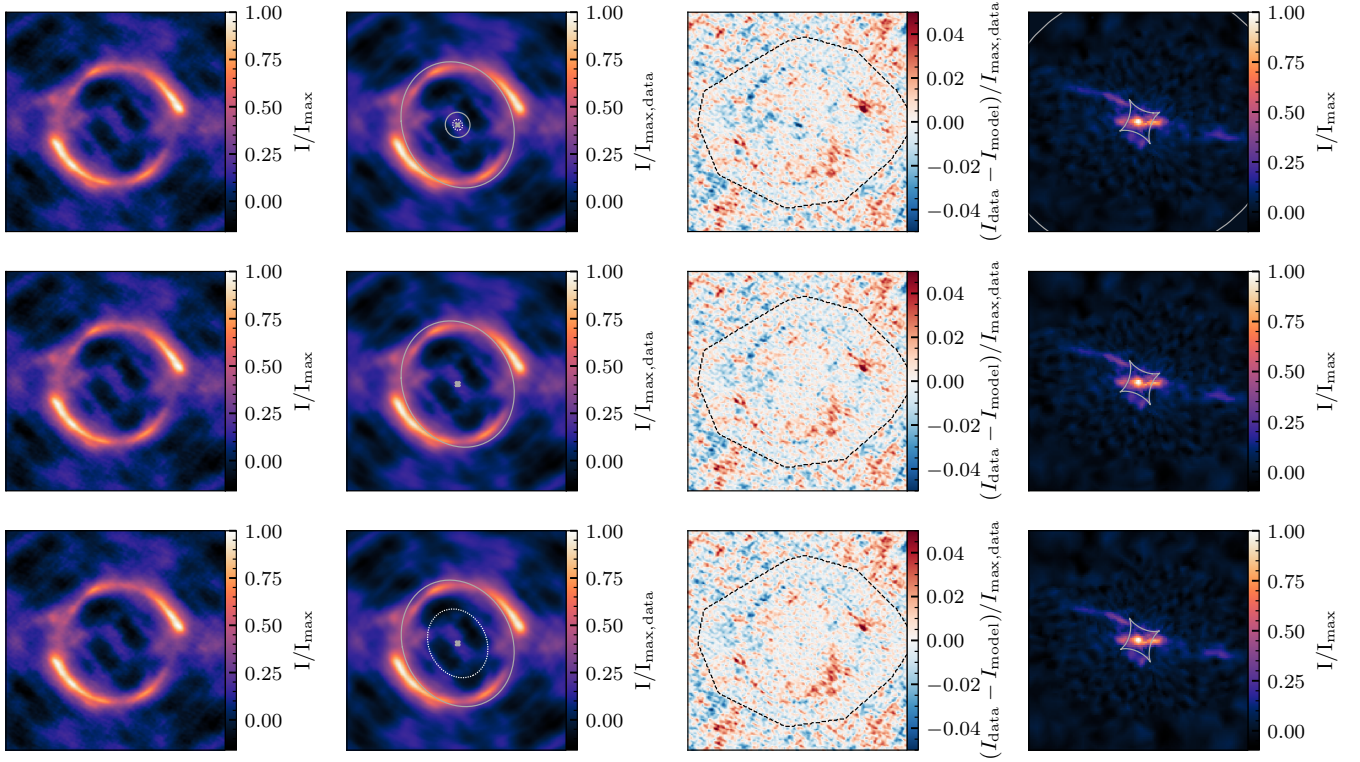


Figure 2. Maximum *a-posteriori* lens models for three parameterisations of the lens mass distribution: PL with fixed core radius of 0.05 arcsec (top row), PL with no core (middle row), and BPL (bottom row). Columns (left to right) show the dirty image of the data, dirty image of the model, residuals, and source. The critical curves and caustics are shown by grey lines on the dirty model and source. The outline of the mask is shown on the residual image. The core or break radius is shown with the dotted white ellipse. Note that the model comparison is done in the uv -plane; these plots are shown only for visualisation.

Table 1. Bayes factor (K) for the models considered, relative to the PL model. Note that the PL+SMBH model produces an unfeasibly large SMBH, so should not be regarded as physically motivated.

model	K
PL ($r_{\text{core}} \equiv 0.05$)	-38
PL	$\equiv 0$
PL + SMBH	1
BPL	16
BPL + SMBH	16

the non-zero external shear preferred for the single power-law is an attempt to account for some angular structure in the lens that can be better fit by a larger central density. Furthermore, for the PL model, the external shear is perfectly aligned with the lens position angle, indicating that it does not represent an external potential.

Including a point mass with the BPL model with a uniform prior in log-space of $10^{6.5} - 10^{9.5} M_{\odot}$ we infer an upper limit on the SMBH of $< 6 \times 10^8 M_{\odot}$ (Fig. 3), consistent with an expected value of $\sim 10^8 M_{\odot}$ from local bulge-SMBH scaling relations for a bulge mass of $10^{10} - 10^{11} M_{\odot}$ (Kormendy & Ho 2013). There is no significant difference in the evidence with the point mass, compared to the BPL-only model. A summary of the marginalised posteriors of the models is given in Table 2 and difference in model evidence is shown in Table 1.

4.2 Stellar mass

We extracted azimuthally averaged surface brightness profiles from the HST data and fit a Sérsic profile (Sérsic 1963) convolved with the PSF. The Python library EMCEE (Foreman-Mackey et al. 2013) was used to perform a Markov Chain Monte Carlo (MCMC) analysis to sample the posterior distributions of the Sérsic profile parameters.

We use the relations of Bell et al. (2003) to estimate a mass-to-light ratio for the stellar component of the galaxy from the near-infrared colour. We find a stellar mass of $6.9 \times 10^{10} M_{\odot}$ for a Salpeter IMF². This is consistent with the mass-size relation for elliptical galaxies at $z \approx 0.75$ and $z \approx 1.25$ found by van der Wel et al. (2014) and extrapolation from the more massive lenses in SLACS (Auger et al. 2010). From the Sérsic fitting we infer a stellar surface mass density ($\Sigma_{\star} = M_{\star} / (2\pi r_{\text{eff}}^2)$) of $1.5 \times 10^9 M_{\odot} \text{ kpc}^{-2}$. These results are summarised in Table 3.

4.3 Hubble constant

We consider implications for the inference of the H_0 with time-delay cosmography for the differences between the PL and BPL models. As shown in Kochanek (2020), the expected fractional error on H_0 (f_{H_0}) can be calculated from the mean convergence at the Einstein radius by

$$f_{H_0} = \frac{H_0^{\text{true}}}{H_0^{\text{model}}} = \frac{1 - \kappa^{\text{true}}(\theta_E)}{1 - \kappa^{\text{model}}(\theta_E)}, \quad (4)$$

² Converted from a Kroupa IMF by diving by a factor of 0.67

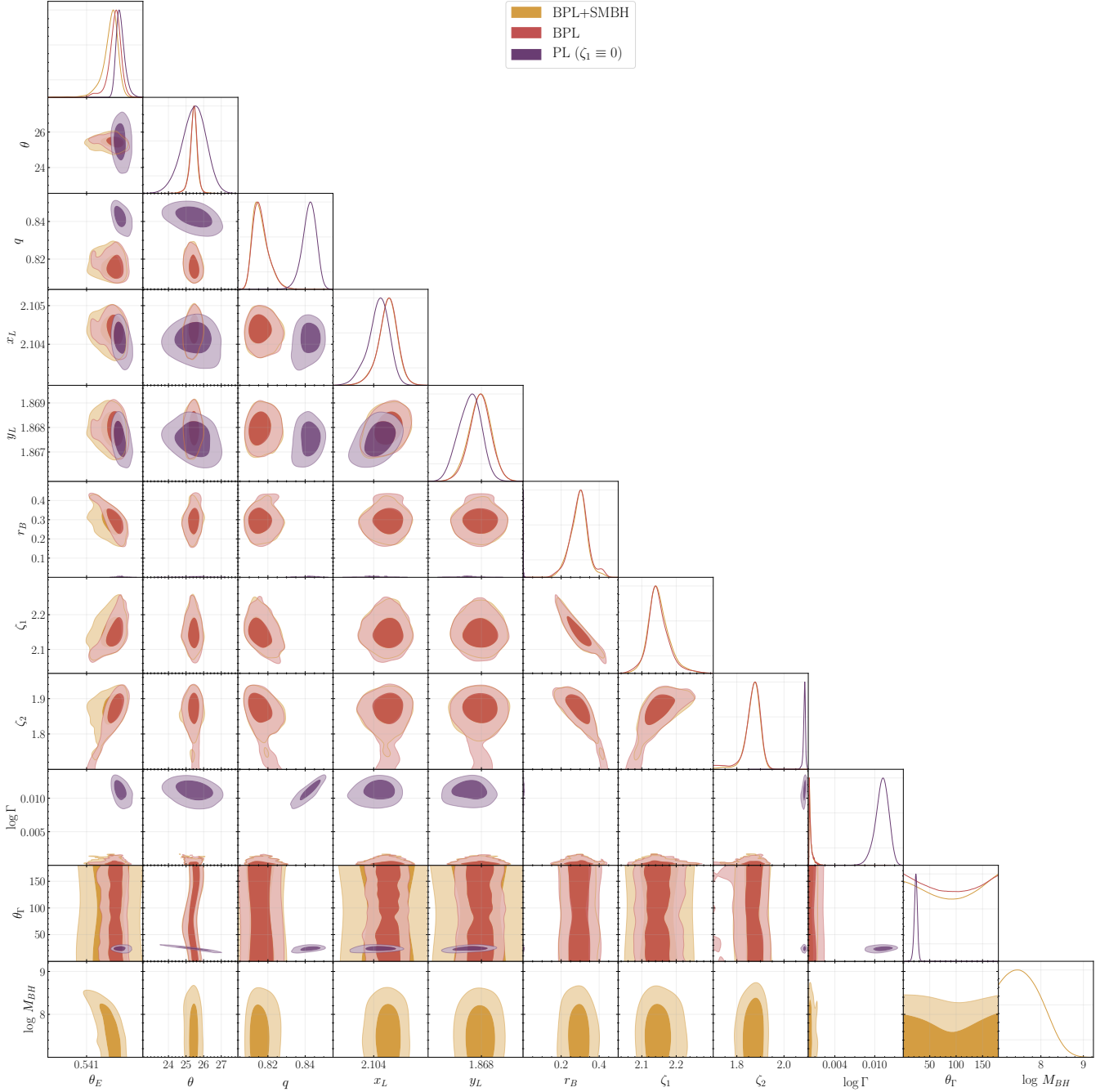


Figure 3. 2-dimensional posterior distributions for the lens parameters for the PL and BPL models obtained with nested sampling. ζ_1 is the inner logarithmic slope and ζ_2 is the outer logarithmic slope (for the PL, ζ_1 is fixed to mimic a core). The BPL model is preferred over the PL model by a Bayes factor of 16.

Table 2. Marginalised posteriors of the lens model parameters obtained with MULTINEST (median, 16th and 84th percentiles). The lens position is relative to the phase centre of the observation. The core radius, break radius and Einstein radius are in units of arcsec. We give the 99.7 percentile as an upper limit on the core radius and SMBH mass.

	x_L	y_L	θ_E	q	θ_q	r_B	ζ_1	ζ_2	Γ	θ_Γ	M_{BH}
PL	$2.1041^{+0.0003}_{-0.0003}$	$1.8675^{+0.0004}_{-0.0005}$	$0.567^{+0.001}_{-0.001}$	$0.843^{+0.004}_{-0.004}$	$25.5^{+0.6}_{-0.7}$	< 0.008	$\equiv 1$	$2.087^{+0.003}_{-0.005}$	$0.0112^{+0.0003}_{-0.0003}$	24^{+3}_{-3}	-
BPL	$2.1044^{+0.0002}_{-0.0003}$	$1.8680^{+0.0004}_{-0.0005}$	$0.5422^{+0.0002}_{-0.0003}$	$0.815^{+0.005}_{-0.003}$	$25.4^{+0.2}_{-0.2}$	$0.30^{+0.04}_{-0.05}$	$2.14^{+0.03}_{-0.02}$	$1.87^{+0.02}_{-0.03}$	< 0.002	0 ± 90	-
BPL+SMBH	$2.1044^{+0.0002}_{-0.0003}$	$1.8679^{+0.0004}_{-0.0004}$	$0.5421^{+0.0002}_{-0.0004}$	$0.815^{+0.005}_{-0.003}$	$25.4^{+0.02}_{-0.02}$	$0.30^{+0.04}_{-0.05}$	$2.15^{+0.03}_{-0.02}$	$1.87^{+0.02}_{-0.03}$	< 0.002	0 ± 90	$< 6 \times 10^8$

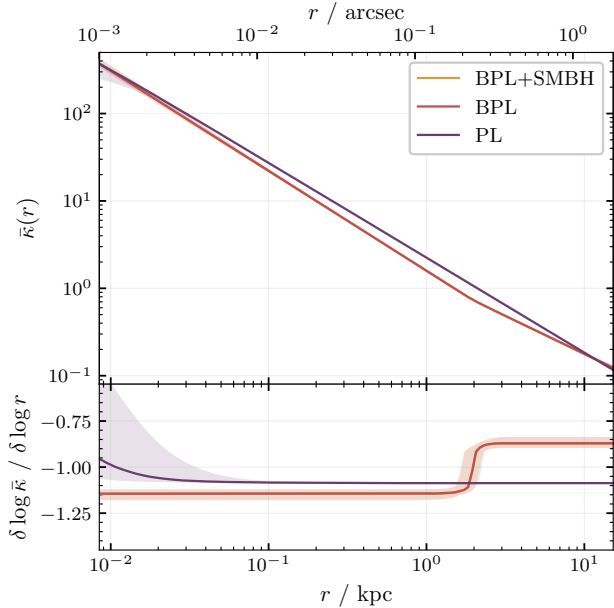


Figure 4. Comparison of the PL, BPL and BPL+SMBH models: (top) the average convergence as a function of radius; (bottom) the logarithmic gradient of the profiles. The solid line is the likelihood-weighted median of 1000 models explored by MULTINEST; the shaded region is the standard deviation. Note that the BPL and BPL+SMBH models completely overlap.

Table 3. Properties of the stellar emission. We give the $r-i$ colour, the stellar effective radius (in arcsec) and Sérsic index for each HST band, the stellar mass derived from the colour for a Salpeter IMF, and the stellar surface mass density ($M_{\odot} \text{ kpc}^{-2}$).

band	$r-i$	r_{eff}	n	$\log M_{\star}$	$\log \Sigma_{\star}$
F160W	0.38	$0.32^{+0.05}_{-0.04}$	3.0 ± 0.2	10.8	9.2 ± 0.1
F110W		$0.32^{+0.06}_{-0.04}$	2.6 ± 0.3		

where $\kappa^{\text{true}}(\theta_E)$ is the convergence of the ground truth at the Einstein radius and $\kappa^{\text{model}}(\theta_E)$ is that of the assumed model. If we take the BPL model as the ground truth, we find that H_0 would be underestimated by 10 ± 1 percent with a single power-law.

5 DISCUSSION

van de Ven et al. (2009) and others have emphasised that strong lens modelling can constrain only the local density profile. Here, we have investigated a lens with an extended lensed source that probes the density across a range of radii. We have used a broken power-law profile to model the gravitational lens SPT 0532–50: the well-constrained inner slope demonstrates that we are able to probe scales much smaller than the Einstein radius.

All analyses which rely solely on lensing data are affected by the mass-sheet degeneracy (MSD). The MSD is a generic feature of the lens equation which allows different mass models to produce the same lensing data (Falco et al. 1985). There are two approaches to breaking the MSD; by combining the lensing data with dynamical constraints, or by assuming a parametric form for the lens galaxy mass profile. The latter is a physically motivated solution to the MSD problem. However, the single power-law model traditionally used in this context is problematic because its parameters can be fit

very precisely even if the underlying galaxy differs significantly from a power-law (e.g. Kochanek 2020). The broken power-law model we use here allows for more flexibility than a single power-law, whilst still simple enough to be constrained by lensing data alone.

The extent of radial arcs into the centre of the galaxy may be an important constraint on the inner density slope. However, it is interesting that the inner slope is still well constrained, while the break radius is inside the radial arcs where there is no lensed emission (see the third row of Fig. 2). This demonstrates that lensing information is not only sensitive to the slope at the location of the lensed images but also at smaller radii. The result is consistent with theoretical work by O’Riordan et al. (2021), who find that the slope of a mass profile truncated inside the lensed images can be recovered for lenses of moderate ellipticity because the shape of the inner mass profile has an effect on the deflection angles everywhere. A BPL model must be tested more widely to determine whether SPT 0532–50 is atypical in its ability to constrain an inner slope.

As demonstrated here, a transition inside the Einstein radius to a super-isothermal slope can erase radial arcs or central images beyond detection (Evans & Hunter 2002). The lack of a central image has frequently been attributed to the effect of the central SMBH (e.g. Wong et al. 2015). If SPT 0532–50 is typical of elliptical lenses, the large scale mass distribution could explain the rarity of detected central images and radial arcs: for example, none of the 22 lenses in the Cosmic Lens All-Sky Survey (CLASS; Browne et al. 2003) have a detected central image at radio frequencies.

A possible implication of the constrained inner slope is the systematic errors on the inference of H_0 with time-delay cosmography. Enzi et al. (2020) found that H_0 would be significantly underestimated if galaxies have flat inner density profiles like those produced in numerical simulations. While we find evidence for a steepening inner slope rather than a core, we would expect 10 percent underestimate in H_0 from a single power-law model. This could indicate significant scatter or bias in cosmographic measurements, potentially exacerbating the tension between lensing and early-Universe measurements of H_0 (Wong et al. 2020). The usefulness of the BPL model for precision lens modelling and implications for H_0 will be investigated systematically in future work.

The total density slopes of the PL and BPL models are close to isothermal, consistent elliptical lenses in the Sloan Lens ACS Survey (SLACS; Auger et al. 2010). As shown in Fig. 5, the slope is consistent with the average total density slopes (0.4–4 times the effective radius) in the IllustrisTNG simulation for elliptical galaxies of similar stellar mass and redshift (Wang et al. 2019). It does not follow the trend of the density slope with redshift, stellar mass and stellar surface density found by Sonnenfeld et al. (2013), which predicts a slope of 1.4 ± 0.2 for the properties of SPT 0532–50 (Fig. 5, dotted black line). Similarly, the redshift evolution of Bolton et al. (2012) predicts a slope of 1.6 ± 0.2 for this lens. However, our result is within the parameter uncertainties for objects at this redshift. A larger sample of high-redshift lenses is needed to determine whether previous tests of the density evolution have been affected by selection bias or other systematic effects (e.g. the environment of the lens or non-zero orbital anisotropy in lens kinematics; Courteau et al. 2014, see also Xu et al. 2017).

It is interesting to consider the selection biases of the lens populations in SLACS, identified on the basis of the lens galaxy velocity dispersion (Bolton et al. 2006), SL2S, discovered via large diameter lensed arcs (Cabanac et al. 2007), and lensed DSFGs, which are identified via the sub-mm flux density of the lensed source emission (e.g. Negrello et al. 2017). The latter selection may result in a different selection of lens galaxy properties. This makes SPT 0532–50

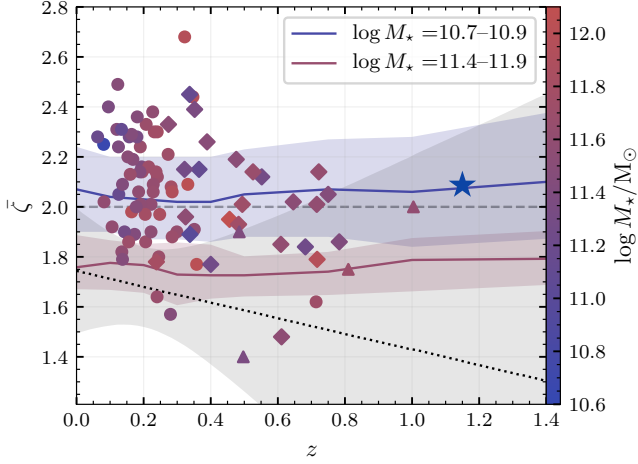


Figure 5. Top: The average total density slope (ζ) as a function of redshift. The circles are SLACS lenses (Auger et al. 2010), the diamonds are SL2S lenses (Sonnenfeld et al. 2013), the triangles are from Treu & Koopmans (2004) and the star this work for the single power-law. The solid lines and shaded regions show the evolution of the slope of elliptical galaxies in the IllustrisTNG simulation (Wang et al. 2019). The dotted black line shows the expected dependence of the slope with redshift and its scatter from Sonnenfeld et al. (2013) for the stellar mass and surface density of SPT 0532–50.

and similar lensed DSFGs interesting targets to widen the parameter space in which to investigate the evolution of elliptical galaxies. A large range of lens redshifts can better probe the evolution of the inner density of ellipticals with time, which have previously been limited to $z \lesssim 0.8$ (Fig. 5) with unknown selection effects. This can test prescriptions of feedback in cosmological simulations (Peirani et al. 2019; Mukherjee et al. 2021) or the growth of galaxies via mergers (Sonnenfeld et al. 2014).

6 CONCLUSIONS

This work represents the first application of a broken power-law model to a real galaxy and demonstrates that lensing alone can constrain the mass distribution inside the lensed images. The strong preference of the SPT 0532–50 data for this model over a single power-law suggests its usefulness for precision lens modelling. Future work will systematically analyse the BPL model and determine the origin of its constraints from lensing data.

For this galaxy, we find the density slope to be in agreement with the evolution of ellipticals in the Illustris TNG simulation. Extending our analysis to a larger sample of sub-mm-selected lenses could probe the cosmic evolution of elliptical galaxies for a broader range redshifts and stellar masses than previously examined. Our results here show that lensing data alone could be sufficient for such a study.

While we have only considered the total density profile here, more complex free-form models would allow us to determine the dark and baryonic contributions to the total density slope. This could help distinguish between Λ CDM and alternative cosmologies. For example, warm dark matter models are expected to produce less concentrated haloes than Λ CDM and produce different populations of low-mass haloes (Lovell et al. 2014). On the other hand, Despali et al. (2019) found that self-interacting dark matter can produce cored or cuspy inner dark matter profiles (where haloes below $\sim 5 \times 10^{12} M_{\odot}$ are more cuspy) but populations of low-mass haloes similar to Λ CDM. Therefore, the combination of measurements of

inner density slopes and the prevalence of low-mass haloes (e.g. Vegetti et al. 2018) could be a powerful tool to differentiate between alternative dark matter models.

ACKNOWLEDGEMENTS

HRS, SV and DMP acknowledge funding from the European Research Council (ERC) under the European Union’s Horizon 2020 research and innovation programme (LEDA: grant agreement No 758853). SV thanks the Max Planck Society for support through a Max Planck Lise Meitner Group. This research made use of Astropy, SciPy, NumPy, Matplotlib and GetDist packages for Python (Astropy Collaboration et al. 2013, 2018; Virtanen et al. 2020; Harris et al. 2020; Hunter 2007; Lewis 2019). We made use of ALMA data with project code 2016.1.01374.S. ALMA is a partnership of ESO (representing its member states), NSF (USA) and NINS (Japan), together with NRC (Canada), MOST and ASIAA (Taiwan), and KASI (Republic of Korea), in cooperation with the Republic of Chile. The Joint ALMA Observatory is operated by ESO, AUI/NRAO and NAOJ.

DATA AVAILABILITY

The data underlying this article will be shared on reasonable request to the corresponding author.

REFERENCES

- Astropy Collaboration et al., 2013, *A&A*, **558**, A33
 Astropy Collaboration et al., 2018, *AJ*, **156**, 123
 Auger M. W., Treu T., Bolton A. S., Gavazzi R., Koopmans L. V. E., Marshall P. J., Moustakas L. A., Burles S., 2010, *ApJ*, **724**, 511
 Begelman M. C., Blandford R. D., Rees M. J., 1980, *Nature*, **287**, 307
 Bell E. F., McIntosh D. H., Katz N., Weinberg M. D., 2003, *ApJS*, **149**, 289
 Birrer S., Amara A., Refregier A., 2016, *J. Cosmology Astropart. Phys.*, **2016**, 020
 Blumenthal G. R., Faber S. M., Flores R., Primack J. R., 1986, *ApJ*, **301**, 27
 Bolton A. S., Burles S., Koopmans L. V. E., Treu T., Moustakas L. A., 2006, *ApJ*, **638**, 703
 Bolton A. S., et al., 2012, *ApJ*, **757**, 82
 Bouché N. F., et al., 2021, arXiv e-prints, p. arXiv:2109.07545
 Browne I. W. A., et al., 2003, *MNRAS*, **341**, 13
 Burkert A., 2020, *ApJ*, **904**, 161
 Cabanac R. A., et al., 2007, *A&A*, **461**, 813
 Collett T. E., et al., 2017, *ApJ*, **843**, 148
 Courteau S., et al., 2014, *Reviews of Modern Physics*, **86**, 47
 Despali G., Sparre M., Vegetti S., Vogelsberger M., Zavala J., Marinacci F., 2019, *MNRAS*, **484**, 4563
 Enzi W., Vegetti S., Despali G., Hsueh J.-W., Metcalf R. B., 2020, *MNRAS*, **496**, 1718
 Evans N. W., Hunter C., 2002, *ApJ*, **575**, 68
 Falco E. E., Gorenstein M. V., Shapiro I. I., 1985, *ApJ*, **289**, L1
 Feroz F., Hobson M. P., Cameron E., Pettitt A. N., 2013, arXiv e-prints, p. arXiv:1306.2144
 Foreman-Mackey D., Hogg D. W., Lang D., Goodman J., 2013, *PASP*, **125**, 306
 Gnedin O. Y., Ceverino D., Gnedin N. Y., Klypin A. A., Kravtsov A. V., Levine R., Nagai D., Yepes G., 2011, arXiv e-prints, p. arXiv:1108.5736
 Grillo C., 2012, *ApJ*, **747**, L15
 Harris C. R., et al., 2020, *Nature*, **585**, 357–362
 Hezaveh Y. D., Marshall P. J., Blandford R. D., 2015, *ApJ*, **799**, L22
 Hunter J. D., 2007, *Computing in Science & Engineering*, **9**, 90
 Keeton C. R., 2003, *ApJ*, **582**, 17
 Kochanek C. S., 2020, *MNRAS*, **493**, 1725

- Kormendy J., Ho L. C., 2013, *ARA&A*, **51**, 511
- Lewis A., 2019, arXiv e-prints, p. [arXiv:1910.13970](https://arxiv.org/abs/1910.13970)
- Lovell M. R., Frenk C. S., Eke V. R., Jenkins A., Gao L., Theuns T., 2014, *MNRAS*, **439**, 300
- Martizzi D., Teyssier R., Moore B., 2013, *MNRAS*, **432**, 1947
- McKean J. P., et al., 2007, *MNRAS*, **378**, 109
- McMullin J. P., Waters B., Schiebel D., Young W., Golap K., 2007, in Shaw R. A., Hill F., Bell D. J., eds, *Astronomical Society of the Pacific Conference Series Vol. 376, Astronomical Data Analysis Software and Systems XVI*. p. 127
- Mukherjee S., Koopmans L. V. E., Metcalf R. B., Tortora C., Schaller M., Schaye J., Varnardos G., Bellagamba F., 2021, *MNRAS*, **504**, 3455
- Muller S., Jaswanth S., Horellou C., Martí-Vidal I., 2020, *A&A*, **641**, L2
- Navarro J. F., Frenk C. S., White S. D. M., 1996, *ApJ*, **462**, 563
- Negrello M., et al., 2017, *MNRAS*, **465**, 3558
- Newman A. B., Treu T., Ellis R. S., Sand D. J., 2013, *ApJ*, **765**, 25
- O’Riordan C. M., Warren S. J., Mortlock D. J., 2020, *MNRAS*, **496**, 3424
- O’Riordan C. M., Warren S. J., Mortlock D. J., 2021, *MNRAS*, **501**, 3687
- Oldham L. J., Auger M. W., 2018, *MNRAS*, **476**, 133
- Peirani S., et al., 2019, *MNRAS*, **483**, 4615
- Pineda J. C. B., Hayward C. C., Springel V., Mendes de Oliveira C., 2017, *MNRAS*, **466**, 63
- Planck Collaboration et al., 2016, *A&A*, **594**, A13
- Pontzen A., Governato F., 2012, *MNRAS*, **421**, 3464
- Powell D., Vegetti S., McKean J. P., Spingola C., Rizzo F., Stacey H. R., 2021, *MNRAS*, **501**, 515
- Quinlan G. D., 1996, *New Astron.*, **1**, 35
- Quinn J., et al., 2016, *MNRAS*, **459**, 2394
- Rizzo F., Vegetti S., Fraternali F., Di Teodoro E., 2018, *MNRAS*, **481**, 5606
- Romano-Díaz E., Shlosman I., Hoffman Y., Heller C., 2008, *ApJ*, **685**, L105
- Rusin D., Ma C.-P., 2001, *ApJ*, **549**, L33
- Rybak M., McKean J. P., Vegetti S., Andreani P., White S. D. M., 2015a, *MNRAS*, **451**, L40
- Rybak M., Vegetti S., McKean J. P., Andreani P., White S. D. M., 2015b, *MNRAS*, **453**, L26
- Sand D. J., Treu T., Smith G. P., Ellis R. S., 2004, *ApJ*, **604**, 88
- Schaller M., et al., 2015, *MNRAS*, **451**, 1247
- Sérsic J. L., 1963, *Boletín de la Asociación Argentina de Astronomía La Plata Argentina*, **6**, 41
- Simon J. D., Bolatto A. D., Leroy A., Blitz L., 2003, *ApJ*, **596**, 957
- Sonnenfeld A., Treu T., Gavazzi R., Marshall P. J., Auger M. W., Suyu S. H., Koopmans L. V. E., Bolton A. S., 2012, *ApJ*, **752**, 163
- Sonnenfeld A., Treu T., Gavazzi R., Suyu S. H., Marshall P. J., Auger M. W., Nipoti C., 2013, *ApJ*, **777**, 98
- Sonnenfeld A., Nipoti C., Treu T., 2014, *ApJ*, **786**, 89
- Sonnenfeld A., Treu T., Marshall P. J., Suyu S. H., Gavazzi R., Auger M. W., Nipoti C., 2015, *ApJ*, **800**, 94
- Tamura Y., Oguri M., Iono D., Hatsukade B., Matsuda Y., Hayashi M., 2015, *PASJ*, **67**, 72
- Treu T., 2010, *ARA&A*, **48**, 87
- Treu T., Koopmans L. V. E., 2004, *ApJ*, **611**, 739
- Vargya D., Sanderson R., Sameie O., Boylan-Kolchin M., Hopkins P. F., Wetzel A., Graus A., 2021, arXiv e-prints, p. [arXiv:2104.14069](https://arxiv.org/abs/2104.14069)
- Vegetti S., Koopmans L. V. E., 2009, *MNRAS*, **392**, 945
- Vegetti S., Despali G., Lovell M. R., Enzi W., 2018, *MNRAS*, **481**, 3661
- Vieira J. D., et al., 2013, *Nature*, **495**, 344
- Virtanen P., et al., 2020, *Nature Methods*, **17**, 261
- Wang Y., et al., 2019, *MNRAS*, **490**, 5722
- Winn J. N., Rusin D., Kochanek C. S., 2004, *Nature*, **427**, 613
- Wong K. C., Suyu S. H., Matsushita S., 2015, *ApJ*, **811**, 115
- Wong K. C., et al., 2020, *MNRAS*, **498**, 1420
- Xu D., Springel V., Sluse D., Schneider P., Sonnenfeld A., Nelson D., Vogelsberger M., Hernquist L., 2017, *MNRAS*, **469**, 1824
- Yoshida N., Springel V., White S. D. M., Tormen G., 2000, *ApJ*, **544**, L87
- de Blok W. J. G., McGaugh S. S., Bosma A., Rubin V. C., 2001, *ApJ*, **552**, L23
- van de Ven G., Mandelbaum R., Keeton C. R., 2009, *MNRAS*, **398**, 607
- van der Wel A., et al., 2014, *ApJ*, **788**, 28